A Multiresolution-Based Method for the Determination of the Relative Resolution between Images: First Application to Remote Sensing and Medical Images

Jorge Núñez,[1,2] Xavier Otazu,[3] María Teresa Merino[1]

[1] Departament d'Astronomia i Meteorologia, Universitat de Barcelona, E-08028 Barcelona, Spain

[2] Observatori Fabra, Reial Acadèmia de Ciències i Arts de Barcelona, Barcelona, Spain

[3] Centre de Visió per Computador, Universitat Autónoma de Barcelona, E-08193 Bellaterra, Spain

Received 13 July 2005; revised 18 July 2005

ABSTRACT: Spatial resolution is a key parameter of all kind of images. This is of particular importance in fields as, for example, medicine or remote sensing. The nominal resolution of a positron emission tomography (PET) or nuclear magnetic resonance (NMR) scanners are directly related to the size, number, and position of the detectors in the scanner ring. Also, the nominal spatial resolution of the remote sensing satellites is a well-known characteristic because it is directly related to the area in ground that represents a pixel in the detector. Nevertheless, in practice, the actual resolution of a medical scanner image or of an image obtained from a satellite is difficult to know precisely because it depends of many other factors. However, if we have two or more images of the same region of interest, obtained using similar or different instruments, it is possible to compare the relative resolution between them. In this paper we propose a wavelet-decomposition-based method for the determination of the relative resolution between two images of the same area. The method can be applied, in principle, to any kind of images. As example, we applied the method to pairs of remote sensing and medical images. In the case of remote sensing, we computed the relative resolution between SPOT-3, LANDSAT-5 and LANDSAT-7 panchromatic and multispectral images taken under similar as well as under very different conditions. In the case of medical imaging, we computed the relative resolution between a pair of simultaneously obtained PET and NMR images of the same object. On the other hand, if we know the true absolute resolution of one of the images of the pair, we can compute the resolution of the other. Thus, in the last part of this paper, we describe a spatial calibrator that we have designed and constructed to help compute the absolute resolution of a single remotely sensed image, presenting an example of its use. Int J Imaging Syst Technol, 15, 225–235, 2005; Published online in Wiley InterScience (www.interscience.wiley.com). DOI 10.1002/ima.20055

Correspondence to: J. Núñez; e-mail: jorge@am.ub.es

Grant sponsors: Ministerio de Ciencia y Tecnología (MCyT) of Spain (nos. AyA2001-3092 and AyA2005-08604). Institut Cartogràfic de Catalunya, Generalitat de Catalunya. Ramón y Cajal, Spanish Ministry of Science and Technology (Xavier Otazu).

Key words: image resolution; wavelet decomposition; relative resolution

I. INTRODUCTION

The spatial resolution is a key parameter for any kind of imaging instruments. This is true regardless of the particular application of the instrument: astronomy, medicine, remote sensing, civil and military patrol, engineering, and so on.

The spatial nominal resolution of many instruments can be derived from their physical characteristics. For example, in satellite-based remote sensing, the nominal resolution is directly related to the area in ground that represents a pixel in the detector. Thus, it is related to the distance from satellite to ground (satellite orbit), pixel size, and focal length of the observing camera or instrument. This nominal resolution has been in constant improvement during the last years (Table I shows the nominal spatial resolution of some of these satellites). In another example, the nominal resolution of a PET scanner is directly related to the diameter of the annulus of detectors of the scanner and to the size, number, and position of the scintillation crystals in the annulus.

However, in practice, the true resolution of an image is also related to many other factors. In the remote sensing example indicated earlier, the true resolution is also related to the size of the point spread function (PSF) of the whole observing system that includes the detector, the optics, the atmospheric conditions, the illumination of the scene, and so on. Also, the atmospheric conditions depend of the quantity of water vapor in the atmosphere, dust in suspension, aerosol concentration, pollution, etc. All these factors are difficult or impossible to know with enough accuracy at any time. In the cited medical example, the true resolution of a scanner image depends, between many other factors, of the type and concentration of the used isotope, the quality of the electronics, the metabolic conditions of the patient, the reconstruction algorithm used, and even the magnetic

Table 1. Nominal spatial resolution of some remote sensing satellites.

	Resolution (m)	
Satellite	Multispectral	Panchromatic
LANDSAT-7	30.0	15.0
SPOT-4	20.0	10.0
SPOT-5	5.0	2.5
IKONOS	4.0	1.0
QuickBird	2.5	0.6

field present during the observation (e.g., during a simultaneous acquisition of PET and NMR images of the same specimen).

Thus, the actual practical spatial resolution of a single image is difficult to know accurately. One method to overcome the problem is to know precisely the size of several features appearing in the image, so we can calibrate the absolute spatial resolution.

However, if we have more than one image of the same region, obtained either by the same or different instruments, it is possible to compare the relative resolution between both images. If we know the absolute resolution of one of them we could compute the resolution of the other. Otherwise, we will have at least a comparison between the quality of both images and its relative resolution. This could be very important in the comparison of, for example, the actual resolution between two different satellite-based platforms or between two different medical scanners.

Another possible application could be to estimate the degree of increment of resolution obtained by a super-resolution method (Park et al., 2003). By computing the relative resolution between the super-resolution result and the images contributing to such result, we could estimate the increment of resolution (super-resolution) achieved.

Thus, in an effort to solve the problem of determining the relative resolution between images, in the first part of this paper, we propose a general wavelet-decomposition-based method for the determination of the relative resolution between two images of the same area. Then, we present examples of application to medical and remote sensing imaging. Also, in the last section we describe the form and use of a spatial calibrator that we have constructed to help to compute the absolute resolution of a single remotely sensed image.

Although, in principle, the method proposed in this paper could be applied to both electronic imaging and digitized classical photography, in practice, digitizing a photographic plate introduces other parameters related to both the photographic process itself (type and density of the emulsion, color or black and white negative, sensitivity, preprocessing, development, etc.) and the digitizing process (type of scanner, physical or interpolated resolution, accuracy of scanning, etc.). These factors beside the nonlinearity of the photographic plate make very difficult the comparison between two different images obtained from digitized photographies unless a complicated system of calibration be carried out. Thus, in this work we will only consider the relative resolution for the case of original digital images obtained, for example, using medical scanners or spatially-based platforms.

II. ALGORITHM FOR ESTIMATING THE RELATIVE RESOLUTION BETWEEN TWO IMAGES

A. Method Outline. The main idea on which the proposed method for evaluating the relative resolution between a pair of images is based consists in the following:

1. Preprocess the images by registering (if needed) the low-resolution image to the same size as the high-resolution one in order to be superimposed, and perform (if needed) a histogram matching between both images.
2. Obtain a series of decreasing resolution versions of the higher resolution image.
3. Compare quantitatively these images with the lower-resolution image of the original pair.
4. Obtain a point of maximum correlation between the images of the series and the low-resolution image of the pair. If we use the higher resolution image to obtain the series and this series is enough long, the correlation should present a maximum.
5. From this maximum compute the relative resolution between the images of the pair.

B. Preprocessing the Images. To carry out the registering and histogram matching, in this work, the images are registered up to within 0.25 pixels rms by resampling the low-resolution image using control points and a bicubic polynomial fit. Also, to take into account the spectral differences (if any), the different atmospheric and illumination conditions, between the two images of the pair, we performed a conventional histogram matching between them. Specifically, after computing the histogram of both images, the histogram of the low-resolution image is used as reference to which we match the histogram of the high resolution one. Of course, if both images were obtained by the same platform under similar conditions this first step could be skipped. Finally, if the number of counts of both images is different, a normalization factor is applied.

This preprocessing was applied in the examples of this work for both the medical and remote sensing cases.

If one of the images of the pair is multispectral and the other is panchromatic, as can be the case in many situations, the best way to compare the relative resolution between both images is to use the intensity component of the multispectral one. This intensity component should be computed in a way such that the result spectrally be as close as possible to the panchromatic image. If both images are multispectral, we can either compare each band of the images one by one (if the bands of both images match), or compute the intensity component of both images as earlier. In the examples of remote sensing in this work, we used the intensity component L of the multispectral images, using the expression $L = \frac{R+G+B}{3}$ with preference to other expressions as $I = \max(R,G,B)$ or $L' = \frac{mxx(R,G,B) + \min(R,G,B)}{2}$. This choice was due to the spectral characteristics of the used images (SPOT-3, LANDSAT-5, and LANDSAT-7).

C. Wavelet Decomposition. To obtain the series of successive lower-resolution versions of the higher resolution image of the pair, we can use several techniques such as, for example, filtering iteratively the image with a low pass filter, e.g., by convolving the image successively with a Gaussian function of known standard deviation. However, in this work, we preferred to use the well-established theory of wavelet decomposition, as described later. This is because we can mathematically know the resolution of each image of the obtained series with respect to the original image.

In the last years, multiresolution analysis has become one of the most promising tools for the analysis of images in all disciplines, particularly in remote sensing (Datcu et al., 1996) and with great incidence in the field of image merging (Yocky, 1995; Ranchin et al.,

1996; Wald et al., 1997; Núñez et al., 1999a, 1999b; González-Audícana et al., 2005; Otazu et al., 2005). Multiresolution analysis based on the wavelet theory allows the introduction of the concept of detail between successive levels of scale or resolution.

Wavelet decomposition is increasingly being used for the processing of images (Chui, 1992; Daubechies, 1992; Meyer, 1993; Young, 1993; Kaiser, 1994; Vetterli and Kovacevic, 1995; Rué and Bijaoui, 1996; Starck and Pantin, 1996; Mallat, 1998). The method is based on the decomposition of the image into multiple channels, based on their local frequency content. The wavelet transform provides a framework to decompose images into a number of new images, each one of them with a different degree of resolution. Although the Fourier transform gives an idea of the frequency content in our image, the wavelet representation is an intermediate representation between the Fourier and the spatial representation, and it can provide good localization in both frequency and space domains. The wavelet transform of a distribution $f(t)$ can be expressed as

$$W(\mathbf{f})(a,b) = |a|^{-1/2} \int_{-\infty}^{+\infty} f(t)\psi\left(\frac{t-b}{a}\right)dt, \qquad (1)$$

where a and b are scaling and translational parameters respectively. Each base function $\psi((t-b)/a)$ is a scaled and translated version of a function ψ called *mother wavelet*. These base functions are $\int \psi((t-b)/a)dt = 0$.

D. The 'à trous' Algorithm. The discrete approach of the wavelet transform can be done with several different algorithms. However, not all algorithms are well suited for all the problems. The popular Mallat's algorithm (Mallat, 1998, 1989) uses an orthonormal basis, but the transform is not shift-invariant, which can be a problem in signal analysis, pattern recognition, or, as in our case, resolution comparison.

To obtain a shift-invariant discrete wavelet decomposition of an image, we follow Starck and Murtagh (1994), and we use the discrete wavelet transform known as "à trous" ("with holes") algorithm (Holschneider and Tchamitchian, 1990) to decompose the image into wavelet planes. Given an image $\mathbf{p}$, we construct the sequence of approximations:

$$F_1(\mathbf{p}) = \mathbf{p}_1, \quad F_2(\mathbf{p}_1) = \mathbf{p}_2, \quad F_3(\mathbf{p}_2) = \mathbf{p}_3, \ldots$$

To construct the sequence, this algorithm performs successive convolutions with a filter obtained from an auxiliary function named scaling function. We use a scaling function that has a $\mathbf{B}_3$ cubic spline profile. The use of a $\mathbf{B}_3$ cubic spline leads to a convolution with a mask of 5×5:

$$\frac{1}{256}\begin{pmatrix} 1 & 4 & 6 & 4 & 1 \\ 4 & 16 & 24 & 16 & 4 \\ 6 & 24 & 36 & 24 & 6 \\ 4 & 16 & 24 & 16 & 4 \\ 1 & 4 & 6 & 4 & 1 \end{pmatrix} \qquad (2)$$

The wavelet planes are computed as the differences between two consecutive approximations $\mathbf{p}_{l-1}$ and $\mathbf{p}_l$. Letting $\mathbf{w}_l = \mathbf{p}_{l-1} - \mathbf{p}_l (l = 1,\ldots, n)$, in which $\mathbf{p}_0 = \mathbf{p}$, we can write the reconstruction formula:

$$\mathbf{p} = \sum_{l=1}^{n} \mathbf{w}_l + \mathbf{p}_r \qquad (3)$$

In this representation, the approximation images $\mathbf{p}_l$ $(l = 0,\ldots,n)$ are versions of the original image $\mathbf{p}$ at increasing scales (decreasing resolution levels), $\mathbf{w}_l$ $(l = 1,\ldots,n)$ are the multiresolution wavelet planes, and $\mathbf{p}_r$ is a residual image. In our case, we are using a dyadic decomposition scheme. Thus, the original image $\mathbf{p}_0$ has double resolution than $\mathbf{p}_1$, the image $\mathbf{p}_1$ double resolution than $\mathbf{p}_2$, and so on. If the resolution of image $\mathbf{p}_0$ is, for example, 10 m, the resolution of $\mathbf{p}_1$ would be 20 m, the resolution of $\mathbf{p}_2$ would be 40 m, and os on. However, note that in this process all the consecutive approximations (and wavelet planes) have the same number of pixels as the original image. This is a consequence of the fact that the "à trous" algorithm is a nonorthogonal oversampled transform (Vetterli and Kovacevic, 1995). This is a restriction on the use of this particular wavelet approach for applications such as image compression.

E. Image Correlation. Once obtained the series of successive lower-resolution versions of the higher resolution image, we proceed to quantitatively compare these images with the lower-resolution image of the original pair. In this work, we performed it by computing the correlation coefficient between the images using the standard coefficient:

$$\mathrm{Corr}(A/B) = \frac{\sum_{j=1}^{n_{\mathrm{pix}}}(A_j - \bar{A})(B_j - \bar{B})}{\sqrt{\sum_{j=1}^{n_{\mathrm{pix}}}(A_j - \bar{A})^2 \sum_{j=1}^{n_{\mathrm{pix}}}(B_j - \bar{B})^2}}, \qquad (4)$$

where $\overline{A}$ and $\overline{B}$ state for the mean value of the corresponding data set. For positive images $-1 < \mathrm{Corr}(A/B) < 1$.

F. Maximum of Correlation. Using Eq. (4), we compute the correlation between each one of the images of the series and the lower-resolution image. The result is a series of correlation numbers which, as stated earlier, if the series is long enough, should present a maximum. For example, if in a remote sensing application, the resolution of the high and low-resolution images of the pair were 10 and 30 m respectively, the series of successive lower-resolution versions of the first image would have resolutions of 10 m (scale 0), 20 m (scale 1), 40 m (scale 2), 80 m (scale 3), and so on. So, the series of correlation numbers between such images and the 30 m image would present a maximum at some point between the 20 and 40 m images of the series.

To compute such maximum, in this work, we fit a cubic spline function to the obtained series of correlation numbers as a function of the scale. Figure 1 shows an example of a correlation curve obtained using real data coming from SPOT-3 (10 m nominal resolution) and LANDSAT-5 (30 m nominal resolution) remote sensing satellites (see examples later). In Figure 1, it is easy to see that, as expected, the maximum of the correlation curve is between scales 1 and 2 (1.585), i.e., between 20 and 40 m.

It is interesting to note here that the series of lower-resolution versions of the higher resolution image could be obtained by other methods as, for example, by Gaussian convolution with a kernel of known Full Width at Half the Maximum (FWHM). In this case a curve similar in form to Figure 1 would be obtained. Figure 2 shows such curve as correlation vs. FWHM of the Gaussian kernel. The maximum of correlation is reached at about FWHM = 3.70. However, as commented later, the relationship between the FWHM of the maximum of the curve and the resolution is not as straight forward to derive as in the case of wavelets.

G. Relative Resolution. As stated earlier, one of the advantages of using the wavelet approach is the dyadic decomposition scheme, which allows an immediate correspondence between the scale of

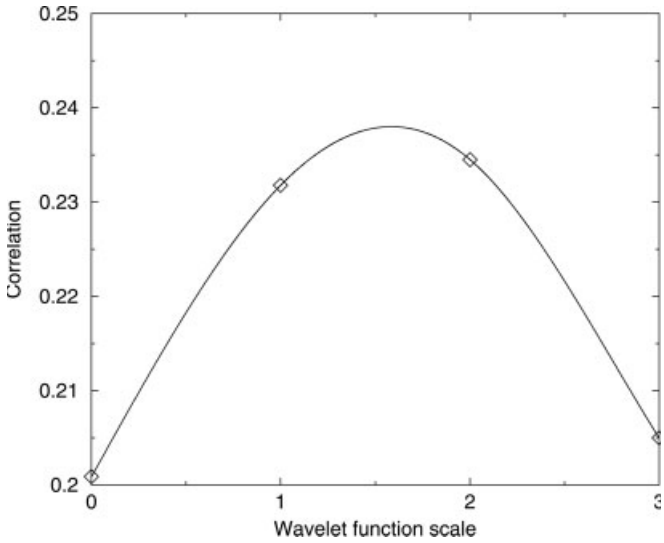

Figure 1. Example of correlation curve between the high and low resolutions images as a function of the scale of the wavelet function.

the decomposition and the resolution. This is a consequence of the properties of the wavelets. Thus, the relationship between the scale of the wavelet decomposition and the relative resolution with regard to the first image of the series (scale 0 or original high resolution image) is:

$$Y = 2^X \tag{5}$$

where X is the scale and Y is the relative resolution between the images of the pair.

In the example of Figure 1, the maximum is for scale = 1.585 that represents a relative resolution of $2^{1.585} = 3.00$ identical in this example to the ratio of nominal resolutions (30 m/10 m = 3) between both images.

Note that in the case of Figure 2 (same data but using Gaussian convolution in place of wavelet decomposition), we do not have a dyadic scheme. So, we cannot use a direct expression as Eq. (5) to compute easily the relative resolution from the FWHM of the maximum of the curve, and an accurate calibration would be needed. This is a consequence of the lack of orthogonal properties of this decomposition scheme.

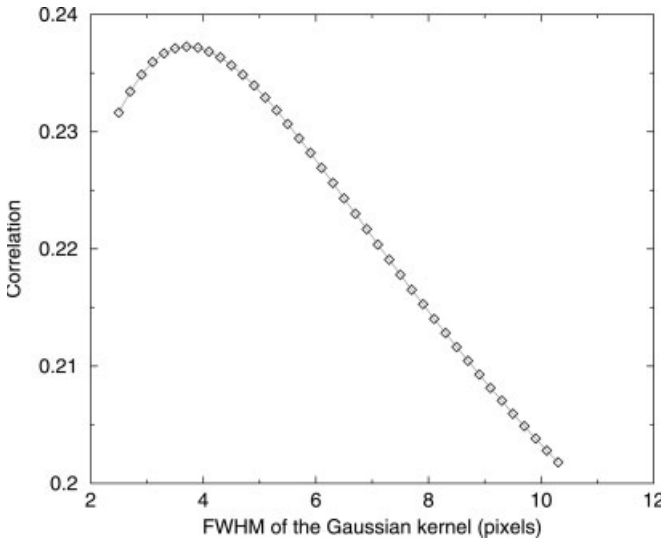

Figure 2. Example of correlation curve between the high and low resolutions images as a function of the FWHM of the Gaussian filter.

III. EXAMPLES OF RELATIVE RESOLUTION

We applied the above methodology to compute the relative resolution between three pairs of images obtained from different sensors. The first example belongs to medical imaging while the other two belong to remote sensing.

A. Application to PET and NMR Medical Images. In the medical imaging example, we computed the relative resolution between a pair of simultaneously obtained Positron Emission Tomography (PET) and Nuclear Magnetic Resonance (NMR) images of the same object. The images were obtained by Paul Marsden and collaborators (Marsden et al., 2002), using a small prototype NMR-compatible PET scanner of their own design. The prototype is capable of acquiring PET images simultaneously with either NMR images or NMR spectra. As described by Marsden et al. (2002) one of the advantages of performing PET and NMR imaging simultaneously is that we can obtain a very good spatial registration of functional PET and anatomical (or functional) NMR images. The possibility to obtain an almost perfect registration (besides the accurate anatomical localization) allows us to use such images for our purpose to compute the relative resolution between them. Of course, images obtained independently by PET and NMR scanners can also be registered but sophisticated software should be used.

Figures 3 and 4 show images of a small hot-spot phantom obtained simultaneously with PET and NMR respectively. Both images are from the paper of Marsden et al. (2002). The PET image

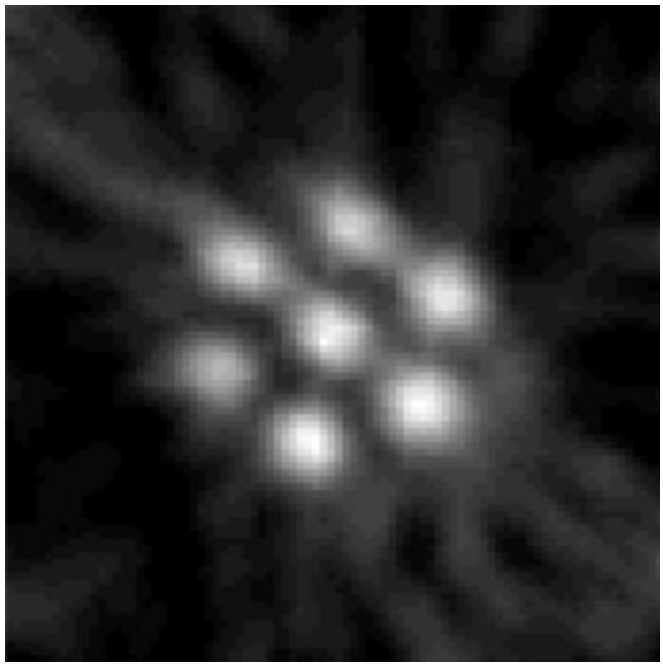

Figure 3. PET image of a small hot-spot phantom obtained by Marsden et al. (2002) using a small prototype NMR-compatible PET scanner. The image was acquired with ^{18}F in 15 min (total counts 300k, activity in phantom 10 MBq). The spot diameter was 2 mm and the separation between spots was 6 mm. The nominal spatial resolution of the scanner is about 2 mm FWHM.

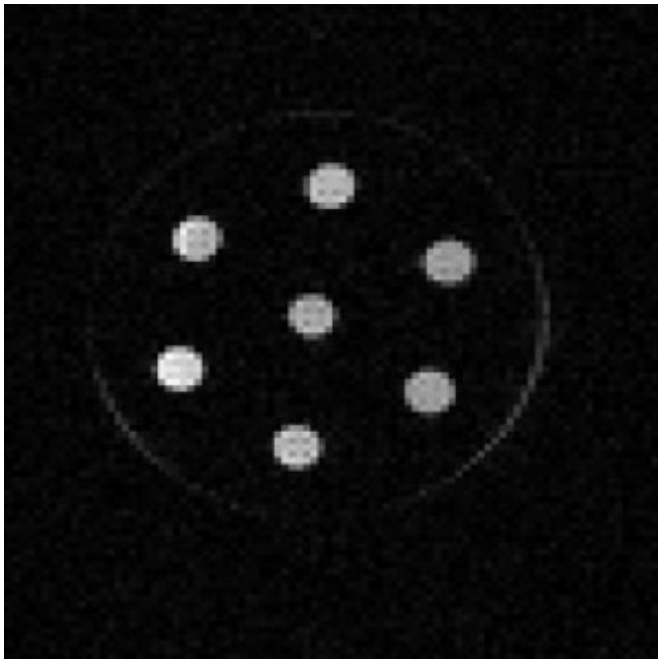

Figure 4. NMR image of the same small hot-spot phantom obtained simultaneously as Fig. 3. The image was acquired on a 4.7T, 30 cm bore system during the same 15 min (spin echo, TE 30 ms, TR 2000 ms).

(Fig. 3) was obtained with ^{18}F in 15 min, with an activity in the phantom of 10 MBq which gives a total of about 300.000 counts. The MR image (Fig. 4) was acquired on a 4.7 T, 30 cm bore system during the same 15 min (spin echo, TE 30 ms, TR 2000 ms). The spot diameter was 2 mm and the separation between spots was 6 mm. The nominal spatial resolution of the PET scanner is about 2 mm FWHM.

The images of Figures 3 and 4 were registered by the method stated earlier, i.e., using control points and a bicubic polynomial fit. Also, we performed a conventional histogram matching between them. Since both images were obtained simultaneously the result of the registration process was very good allowing to apply the algorithm to compute the relative resolution.

Following the above described methodology, we used the wavelet decomposition to obtain a series of lower-resolution images of the NMR image, we used Eq. (4) to compute the correlation of each image of the series with respect to the PET image and we fitted a cubic spline to the set of correlations. Figure 5 shows the obtained curve.

The curve in Figure 5 presents, as expected, a maximum. The maximum correlation is about 0.85. The maximum of the correlation of Figure 5 corresponds to a wavelet scale of 4.33. Applying Eq. (5), we computed the relative resolution of the pair as 19.97.

Since the nominal spatial resolution of the PET scanner is about 2 mm FWHM, the result means that, in this example, the spatial resolution of the NMR image was 20 times higher i.e., about 0.1 mm (100 μm). This result is in good agreement with the high (sub-mm) spatial resolution of a 4.7 T, NMR 30 cm bore system acquiring during 15 min.

Of course this result does not imply in any way that the NMR scanner is better than the PET one since both are observing different functional and anatomical images.

On the other hand, it has been published results using both simulations (Iida et al., 1986) and experimental measurements (Hammer et al., 1994) that the reduction in positron range that occurs in a strong magnetic field could in principle lead to an improvement in the resolution obtainable with a PET scanner. So, if the true spatial resolution of the NMR scanner is well known, the presented method can help to further study this effect on the spatial resolution on PET images.

B. Application to Remote Sensing Images. In the remote sensing examples, the first pair of images was obtained by the same satellite (LANDSAT-7) during the same passage, but using two different instruments. They show a detail of the Italian city of Naples showing, thus, an urban area. Figure 6 shows the high resolution image of the pair. It was obtained using the panchromatic sensor which has a nominal spatial resolution of 15 m. The low-resolution image corresponds to the multispectral sensor of the satellite, which has a nominal spatial resolution of 30 m. To compare its resolution with respect to the panchromatic image, we transformed this image to panchromatic, considering only the intensity component, which was computed as the mean of the first three channels (1, 2, 3) of the multispectral image. Figure 7 shows the low-resolution image (30 m) once transformed to panchromatic. Of course, both images of the pair belong to the same epoch of the year and present the same conditions of illumination.

A very different situation is shown in the second pair of images. They show a nonurban area observed from different satellites in different epoch of the year. The images show a detail of an Argentinean landscape, which includes several agricultural lots, roads, a river bed, and a small town. Figure 8 shows the high resolution image of the pair which is a 10 m resolution panchromatic image obtained by the SPOT-3 satellite. The corresponding low-resolution image of the pair is displayed in Figure 9. It was obtained with the multispectral sensor of the LANDSAT-5 satellite, which has a nominal spatial resolution of 30 m. As in the previous pair, to compare its resolution with respect to the high resolution panchromatic image, we transformed this image to panchromatic, using the intensity component of the image. In this case, the intensity component was computed as the mean of the three (R, G, B) pseudochannels, which

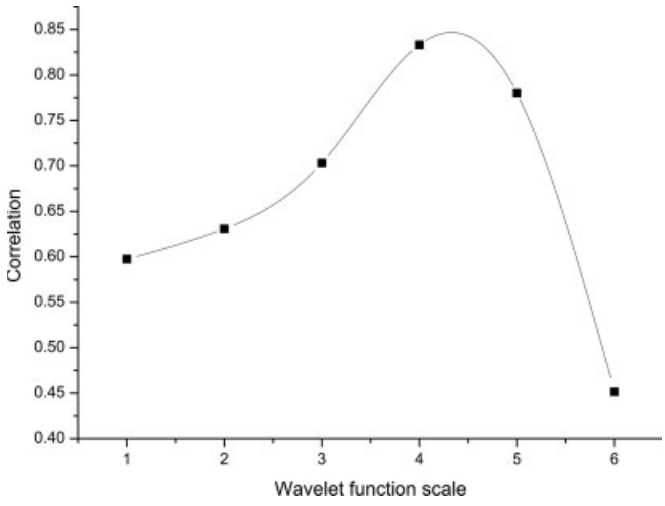

Figure 5. Correlation curve between the NMR and PET images displayed in Figs. 4 and 3, as a function of the scale of the wavelet function.

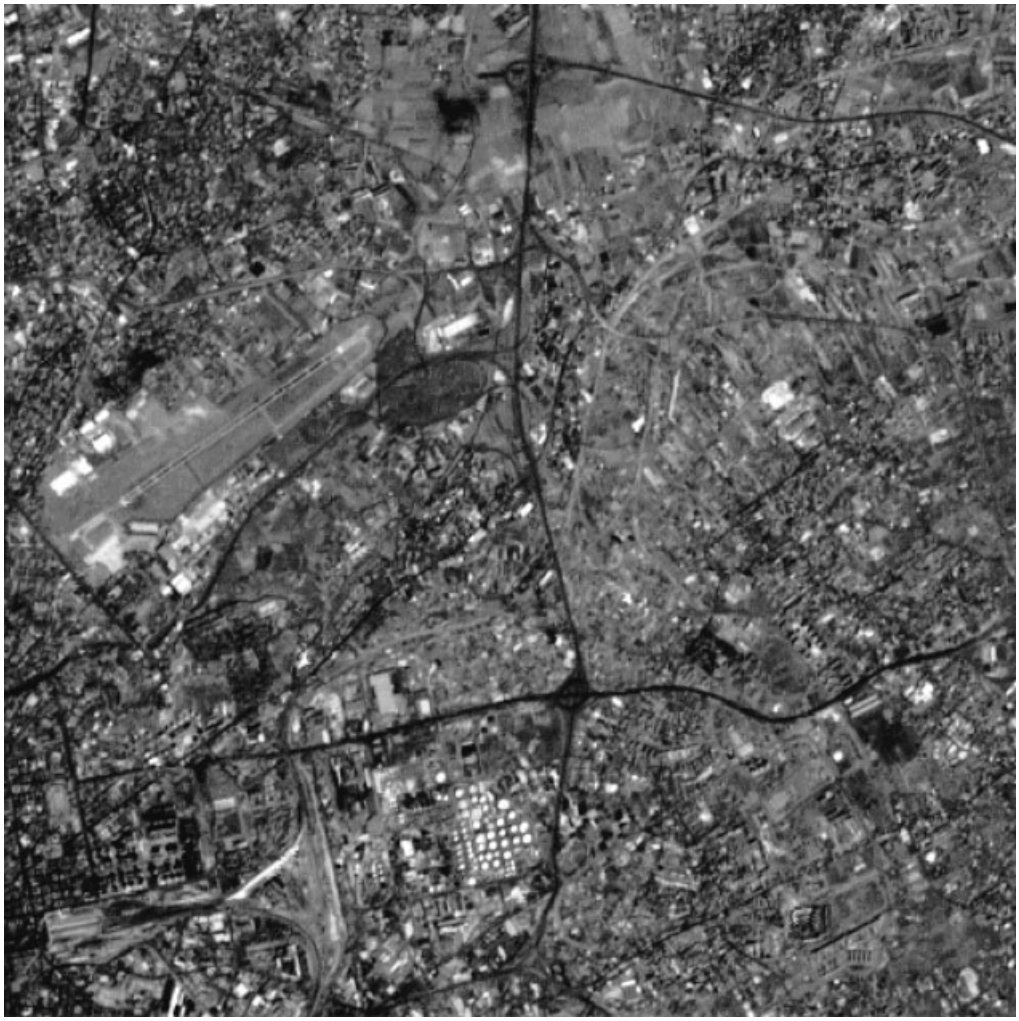

Figure 6. High resolution (15m) panchhromatic image of Naples obtained by the LANDSAT-7 satellite.

were previously computed using the usual transformation: $R = \frac{B_5+B_7}{2}$, $G = \frac{B_3+B_4}{2}$, $B = \frac{B_1+B_2}{2}$. In Figures 8 and 9 it is easy to see that the SPOT-3 and LANDSAT-5 images were taken at different epochs as it is usual when working with images from different satellites. Note, for example, the aspect of the bed of the river, the water ponds (black rounded areas in the LANDSAT image) or the crop fields, which in the SPOT image are clearly different from their appearance in the LANDSAT image. Also, there are several features in the SPOT picture that were not present when the LANDSAT image was taken.

The registering between the two images of each pair was carried out, as stated earlier, resampling the low-resolution image using control points and a bicubic polynomial fit. Also, to compensate the spectral differences between the images, we performed a histogram matching between the two images of each pair using the histogram of the low-resolution image as reference to match the histogram of the high resolution one.

Following again the aforementioned method, we used the wavelet decomposition to obtain a series of lower-resolution images of the high resolution image for each pair, we used Eq. (4) to compute the correlation of each image of the series and the corresponding low-resolution image, and we fitted a cubic spline to each set of correlations. Figures 10 and 11 show the obtained curves. Note that Figure 11 is the same as Figure 1, but we repeat the figure here for completeness.

As expected, both curves present a maximum. The maximum correlation reached in both examples is, however, different: in the first example the maximum correlation is about 0.59, while in the second is about 0.24. This is a logic consequence of the different type of images involved in the presented examples: while in the first example both images come from the same satellite under same conditions, in the second example they come, as commented above, from different satellites under very different conditions.

The maximum of the correlation of Figure 10 corresponds to a scale of 1.083, while the maximum in Figure 11 is at scale 1.585. Applying Eq. (5), we computed the relative resolution of each pair as 2.12 and 3.00, respectively.

The computed relative resolution of the first example (2.12) is close but slightly higher than the nominal which is 2 (30 m vs. 15 m nominal resolutions of both sensors of the LANDSAT-7 satellite). This difference can be due to several effects. Since both images of the pair were obtained under the same observing conditions by the same satellite, the most plausible reason could be that the multispectral camera has an actual spatial resolution slightly worst than nominal, although other explanations could be also present. Since the proposed method can only compute the relative resolution is not possible to know accurately the origin of this difference.

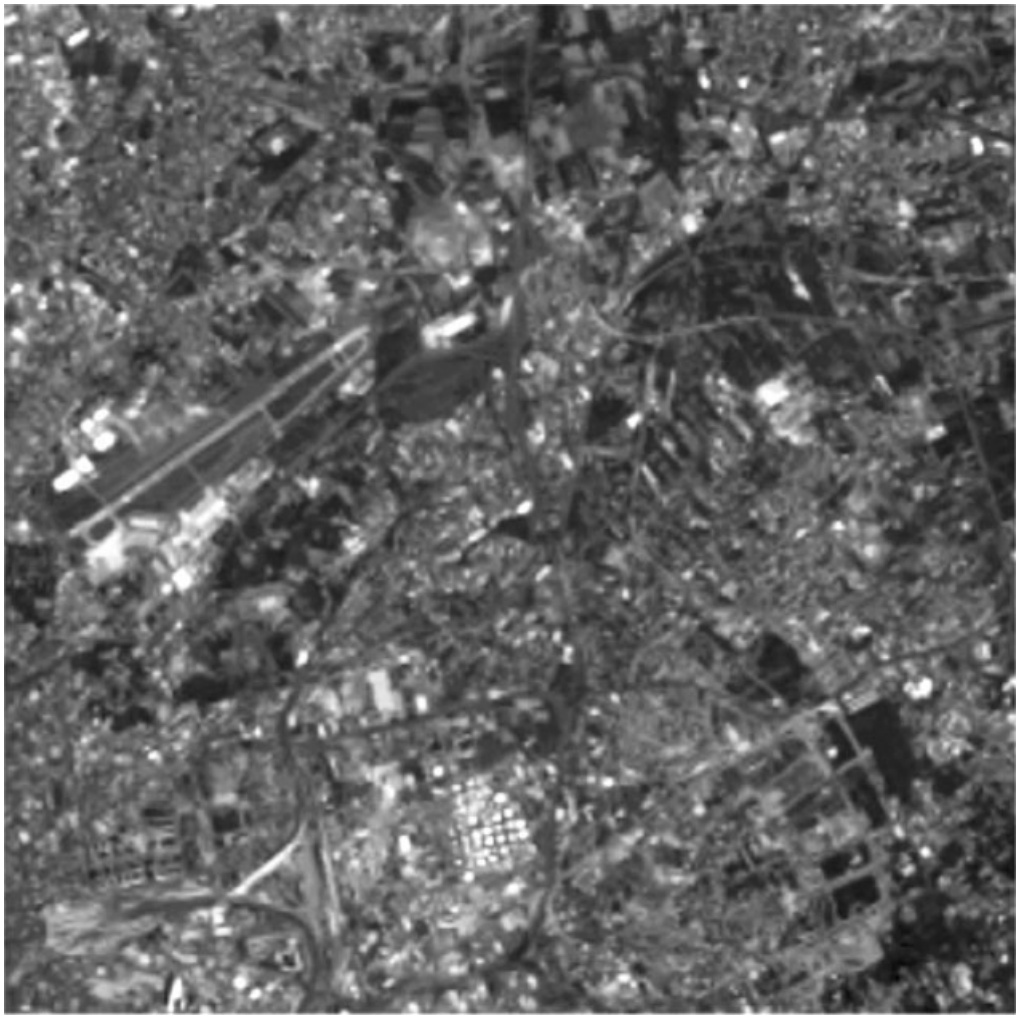

Figure 7. Low resolution (30m) multispectral image of the same area as Fig. 6 obtained simultaneously as Fig. 6 by the LANDSAT-7 satellite. The image was transformed to intensity levels.

In the case of the second example, we obtained a relative resolution (3.00) identical to the nominal one which is 3 (30 m vs. 10 m nominal resolutions of LANDSAT5 and SPOT3 satellites). We believe this result could be due to chance because, even accepting that both SPOT-3 and LANDSAT-5 satellites could give exactly their nominal resolution, the different observing conditions should make at least small differences in the actual resolution of the images.

Additional details about these remote sensing examples, including an analysis by spectral bands, can be found in Núñez et al. (2006).

From these results, we can conclude that the proposed method shows a good performance when estimating the relative resolution between remotely sensed images, not only under ideal conditions but even under quite different circumstances as different satellites, different epoch of the year and different type of images (panchromatic and multispectral) as in the last example.

IV. SPATIAL ABSOLUTE CALIBRATOR FOR REMOTE SENSING

The method developed in previous sections allows estimating the relative resolution between two images, but we cannot compute the absolute resolution of them. As stated earlier, the actual spatial resolution of an image is difficult to know precisely and the best way to estimate it is to know the size of a set of features appearing in the image in order to calibrate its absolute spatial resolution. This can be easy in disciplines in which it is possible to construct and observe a spatial calibrator as is the case of the small hot spot phantom displayed in the medical example above, but can be difficult in other disciplines as remote sensing in which such calibrators are not common.

In this section, we describe a spatial calibrator that we have constructed to help to compute the absolute resolution of a single remotely sensed image. The calibrator, which is painted on the terrace of the Physics Department of the University of Barcelona, consists in two series of parallel fringes of decreasing width and a series of triangles with a common vertex. One of the series of parallel fringes is in direction North–South and the other in direction East–West, so we can calibrate the resolution in both directions. The fringes are painted alternatively in white and red color. We use the red color in place of black to facilitate the use of the calibrator when using multispectral observations. The total size of the calibrator is 18×6 m^2 divided in three squares of 6×6 m^2 (one for each group of fringes and one for the triangles). The width of the fringes are 100, 90, 80, 70, 60, 50, 40, 30, and 20 cm and 6 fringes of 10 cm. Each triangle is a rectangle triangle of 300 cm basis. The size of the whole calibrator and the width of the fringes were chosen in order to be useful for both observations from airborne sensors and for high resolution satellites as SPOT-5, IKONOS, Quickbird and other future platforms.

Figure 8. High resolution (10m) panchhromatic image of an Argentinean scene obtained by the SPOT-3 satellite.

Figure 12 shows an outline of the calibrator and Figure 13 a real observation of it taken from an airborne panchromatic camera. The calibrator is located at World Geodetic System coordinates (WGS84) $\lambda = 2^\circ 7' 4.1'' \text{ E}$; $\phi = 41^\circ 23' 4.4'' \text{ N}$; $h = 95$ m HMSL.

The calibrator can be used in different ways. We use two criteria to compute the resolution.

Since the width of fringes is variable, the first criterion is simply to see up to which width it is possible to solve the fringes or the additional triangles in the image. Using this criterion, we can compute resolutions between 300 cm (the basis of the triangles) and 10 cm (the minimum width of the fringes).

If the spatial resolution is higher than 10 cm, i.e., even all the smallest fringes (10 cm) are solved in the image (presently only airborne sensors can achieve this), we apply the second criterion to estimate the resolution. This is based in the Rayleigh criterion, which establishes that two punctual sources are solved if the center of their PSFs is separated more than the radius of the same PSF. In our case, this criterion is translated into computing the intensity profile of a line perpendicular to the fringes and to study the transition zone between two consecutive fringes. We define the resolution of the image as the distance at which the intensity of a white fringe drops a half of the intensity difference with regard to the adjacent dark fringe.

Figure 14 illustrates the second estimation criterion. Figure 14 is a detail of an image similar to Figure 13, it shows a dark fringe between two white ones and the intensity profile along a line perpendicular to them. It is easy to see that the intensity of the white fringe drops a half of the difference between adjacent fringes at about 4.5 pixels. To compute the corresponding resolution we need also the scale of the image, but since we know the true size of the fringes, computing the scale in cm/pixel is straightforward.

Figure 13 also illustrates that the calibrator can be used to detect differences of resolution in different directions due to problems in the optics or to errors in the motion compensator. Note that, in Figure 13, the resolution in E–W direction (horizontal) is clearly worse than that in the N–S direction (vertical). It can be easily seen because the 10 cm horizontal fringes at left are clearly visible while the 10 cm vertical fringes at center-right are not. This is probably due to a bad calibration of the motion compensator of the airborne camera which took the image. In a case like this, we can use the first criterion above to estimate the resolution in the E–W direction and the second one for the N–S direction. In this particular example, we obtained about 10 cm resolution in the E–W direction but better than 5 cm resolution (applying second criterion) in the N–S direction.

We should note that, since the calibrator is located at a fixed place, its use is, in principle, restricted to calibrate observations that include it. However, given that remote sensing satellites can observe an specified area as many times as desired, it is possible to use the calibrator to obtain the true resolution of a series of images taken

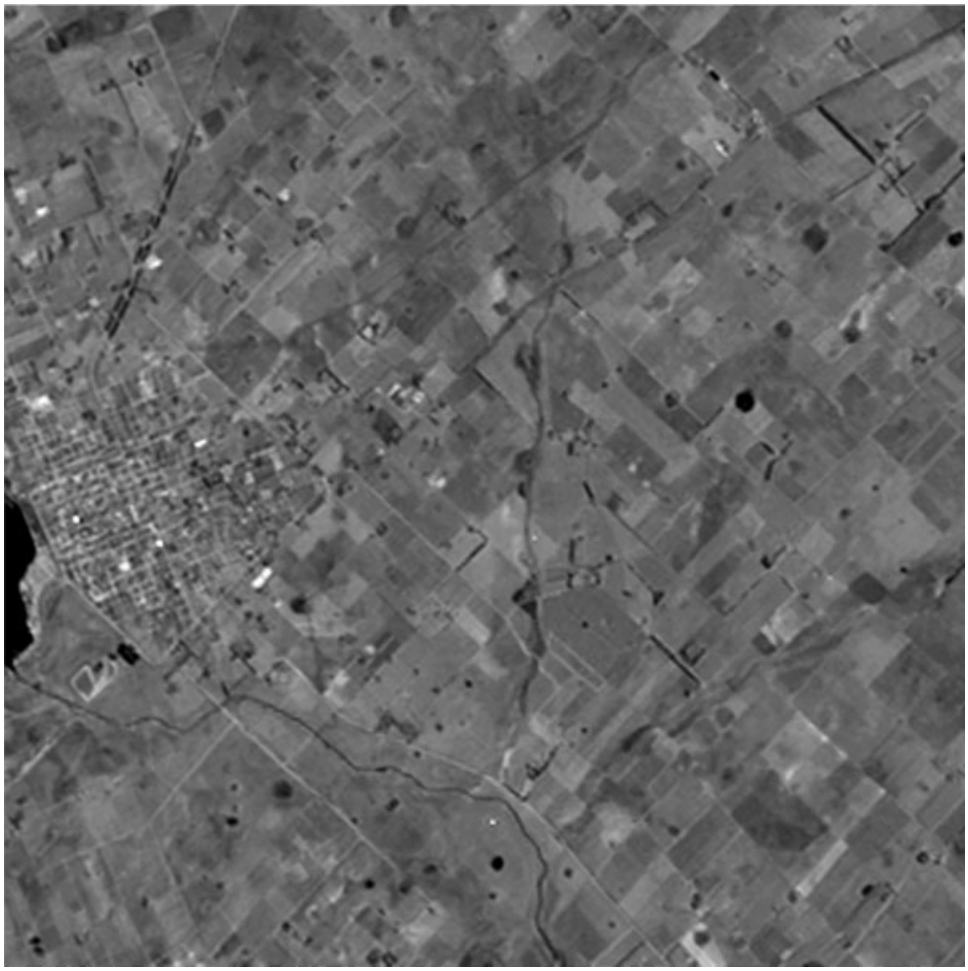

Figure 9. Low resolution (30m) multispectral image of the same area as Fig. 8 obtained by LANDSAT-5 satellite. The image was transformed to intensity levels. Figs. 8 and 9 were obtained during different epochs of the year.

under different conditions of illumination, dust, pollution or weather. This can help to better calibrate the actual resolution of the satellite under such conditions or to calibrate a possible malfunction of the satellite. The combination of this true resolution calibration and the relative resolution computation presented above can help to better estimate the absolute resolution of any image in remote sensing.

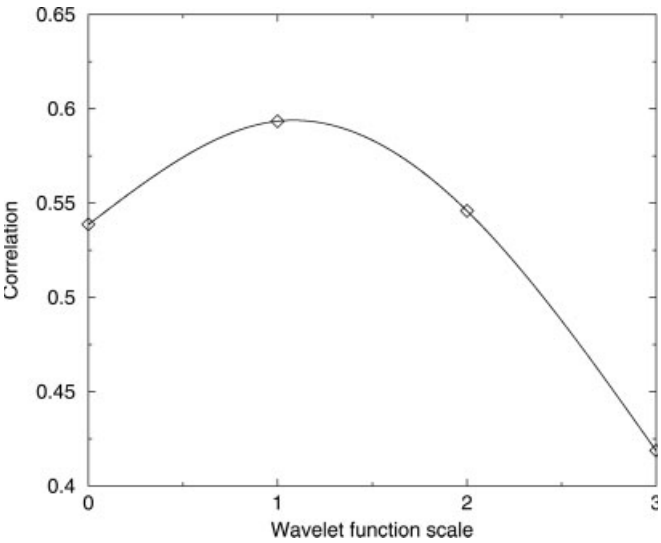

Figure 10. Correlation curve between the high and low resolutions images displayed in Figs. 6 and 7, as a function of the scale of the wavelet function.

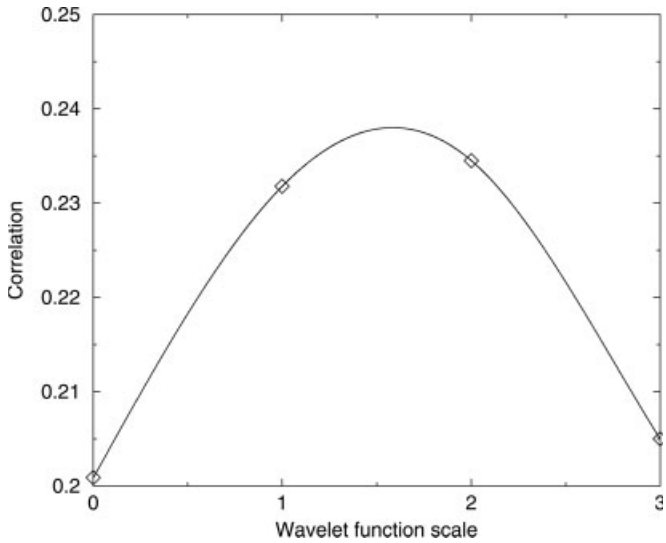

Figure 11. Correlation curve between the high and low resolutions images displayed in Figs. 8 and 9, as a function of the scale of the wavelet function.

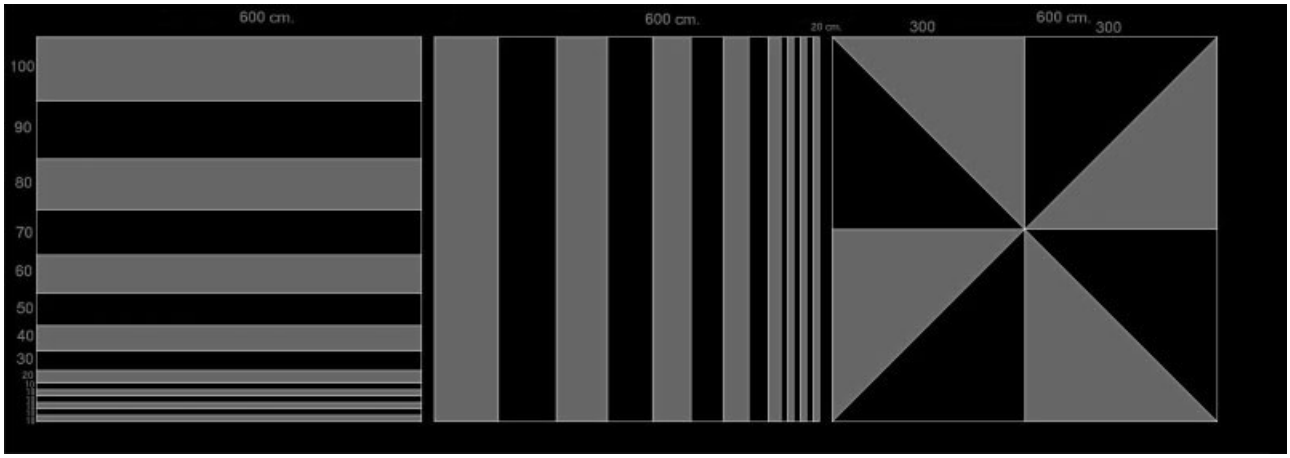

Figure 12. Outline of the calibrator designed to estimate the absolute resolution of remotely sensed images.

V. CONCLUSIONS

The actual spatial resolution of an image is a key parameter, but difficult to know with high accuracy. The main aim of this paper was to establish a method for estimating the relative resolution between images showing its applicability over a very different types of them (medicine and remote sensing). Also we propose a calibrator to estimate the absolute resolution in the case of remote sensing.

The proposed relative method, useful for the determination of the relative resolution between two images of the same object or area, is based in the mathematical properties of the wavelet decomposition, in particular in the dyadic properties of the "à trous" algorithm of wavelet decomposition. The proposed method obtains the relative resolution from the computation of the maximum of the correlation between a series of images of decreasing resolution of the high resolution image and the lower-resolution image of the pair. The method works well with panchromatic and multispectral images.

To show the power of the method, we applied it to three very different pairs of images belonging to medicine and remote sensing.

In the medicine example, the pair of images were a PET and a NMR images of the same object obtained simultaneously by a NMR compatible PET scanner, which allows a good registration between them. We computed accurately the relative resolution between the images of the pair concluding that the proposed method is enough robust to estimate the relative resolution between such different kind of images. We also show that the method can help to better measure some properties of these images as, for example, the increment of spatial resolution of PET images taken under strong magnetic fields.

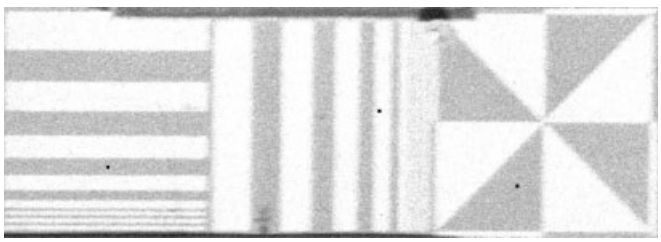

Figure 13. Real observation of the calibrator obtained from an airborne panchromatic camera. The calibrator is located at WGS84 coordinates: $\lambda = 2\ 7\ 4.1\ E$; $\phi = 41\ 23\ 4.4\ N$; $h = 95m$ *H M S L.* Note the different spatial resolutions in E-W and in N-S directions.

In the remote sensing examples, one of them was a pair of images obtained by the panchromatic and multispectral sensors of the LANDSAT-7 satellite under identical conditions. The other pair was composed by a panchromatic image obtained by the SPOT-3 satellite and a multispectral image obtained at different epoch of the year by the LANDSAT-5 satellite, thus under very different conditions. In both cases we computed accurately the relative resolution between the images of the pair. Thus, we can conclude that the method is also robust in estimating the relative resolution between remotely sensed images, not only under ideal conditions but even for different satellite and under different circumstances as epoch of the year and spectral characteristics of the images.

Since the proposed method can only estimate relative resolution, in the last part of this paper we presented the design, characteristics, and use of a spatial calibrator for remote sensing that we constructed on the terrace of our Department. Its design helps to compute the absolute resolution of an image in both N–S and E–W directions, allowing to detect possible differences in resolution with direction. Its size makes it useful for both airborne sensors and high resolution satellites. The calibrator can be used to better establish

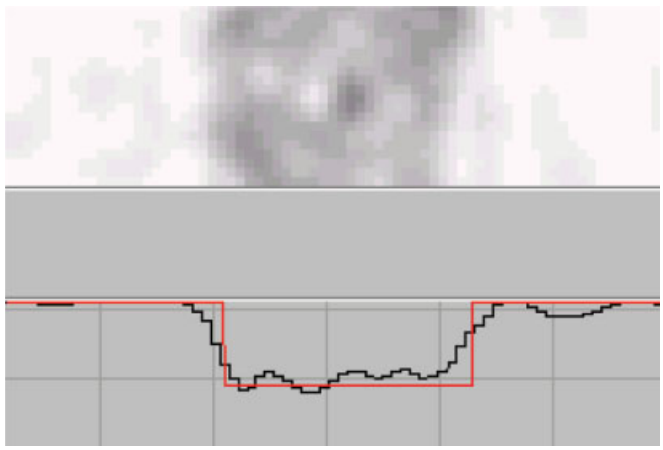

Figure 14. Illustration of the Rayleigh criterion to compute the absolute resolution of an image. The figure shows a dark fringe of the calibrator between two white ones and the intensity profile along a line perpendicular to them. [Color figure can be viewed in the online issue, which is available at www.interscience.wiley.com]

the actual resolution of a satellite under different conditions of weather, illumination, pollution, etc., and to detect possible malfunctions of the satellite. To use the calibrator we presented a direct estimation method, and another method based on Rayleigh criterion, which allows to compute absolute resolutions from 3 m to few cm. We presented a real example of its use that allowed us to detect appreciable differences in resolution in E–W and N–S directions.

Finally, the combination of the relative and absolute methods presented in this paper can help to estimate the absolute resolution of any image.

REFERENCES

C.K. Chui, An Introduction to wavelets, Academic Press., Boston, 1992.

M. Datcu, D. Luca, and K. Seidel, Multiresolution analysis of SAR images, EUSAR'96, Konigswinter, Germany, 1996, pp. 375–378.

I. Daubechies, Ten lectures on wavelets, SIAM Press, Philadelphia, 1992.

M. González-Audícana, X. Otazu, O. Fors, and A. Seco, Comparison between the Mallat's and the à *trous* discrete wavelet transform based algorithms for the fusion of multispectral and panchromatic images, Int J Remote Sensing 26 (2005) 597–616.

B.E. Hammer, N.L. Christensen, B.G. Heil, Use of a magnetic-field to increase the spatial-resolution positron emission tomography, Med Phys 21 (1994) 1917–1920.

M. Holschneider and P. Tchamitchian, In P.G. Lemarié (editor), Les ondelettes en 1989, Springer-Verlag, Paris, 1990, p. 102.

H. Iida, I. Kanno, S. Miura, M. Murakami, K. Takahashi, and K. Uemura, A simulation study of a method to reduce positron-annihilation spread distributions using a strong magnetic-field in positron emission tomography, IEEE Trans Nucl Sci 33 (1986) 597–600.

G. Kaiser, A friendly guide to wavelets, Birkhauser, Boston, 1994.

S. Mallat, A theory for multiresolution signal: the wavelet representation, IEEE Trans Pattern Anal Mach Intel 11 (1989) 679–693.

S. Mallat, A wavelet tour of signal processing, 2nd edition, Academic Press, San Diego, 1998.

P.K. Marsden, D. Strul, S.F. Keevil, S.C.R. Williams, and D. Cash, Simultaneous PET and NMR, Br J Radiol 75 (2002) S53–S59.

Y. Meyer, Wavelets: Algorithms and applications, SIAM Press, Philadelphia, 1993.

J. Núñez, X. Otazu, O. Fors, V. Palà, and R. Arbiol, Multiresolution-based image fusion with additive wavelet decomposition, IEEE Trans Geosci Remote Sens 37 (1999a) 1204–1211.

J. Núñez, X. Otazu, O. Fors, A. Prades, V. Palá, and R. Arbiol, Image fusion using additive multiresolution wavelet decomposition. Applications to SPOT + LANDSAT images, J Opt Soc Am A 16 (1999b) 467–474.

X. Otazu, M. González-Audícana, O. Fors, and J. Núñez, Introduction of sensor spectral response into image fusion methods. Application to wavelet based methods, IEEE Trans Geosci Remote Sens 93 (2005) 2376–2385.

J. Núñez, O. Fors, X. Otazu, V. Palà, R. Arbiol, and M.T. Merino, A wavelet-based method for the determination of the relative resolution between remotely sensed images, IEEE Trans Geosci Remote Sens 44 (2006), to appear.

S.C. Park, M.K. Park, and M.G. Kang, Super-resolution image reconstruction: A technical overview, IEEE Signal Process Mag 20 (2003) 21–36.

T. Ranchin, L. Wald, and M. Mangolini, The ARSIS method: A general solution for improving spatial resolution of images by the means of sensor fusion, In T. Ranchin and L. Wald (editors), Proceedings of the International Conference: Fusion of Earth Data, Cannes, France, 1996, pp. 53–58.

F. Rué and A. Bijaoui, A multiscale vision model applied to astronomical images, Vistas Astron 40 (1996) 495–502.

J.L. Starck and F. Murtagh, Image restoration with noise suppression using the wavelet transform, Astron Astrophys 288 (1994) 342–350.

J.L. Starck and E. Pantin, Multiscale maximum entropy image restoration, Vistas Astron 40 (1996) 563–569.

M. Vetterli and J. Kovacevic, Wavelets and subband coding, Prentice Hall, Englewood Cliffs, NJ, 1995.

L. Wald, T. Ranchin, and M. Mangolini, Fusion of satellite images of different spatial resolution: assessing the quality of resulting images, Photogramm Eng Remote Sens 63 (1997) 691–699.

D.A. Yocky, Image merging and data fusion by means of the discrete two-dimensional wavelet transform, J Opt Soc Am A 12 (1995) 1834–1841.

R.K. Young, Wavelet theory and its applications, Kluwer Academic, Boston, 1993.